

# Inhibiting amyloid- $\beta$ cytotoxicity through its interaction with the cell surface receptor LirB2 by structure-based design

Qin Cao<sup>1</sup>, Woo Shik Shin<sup>2</sup>, Henry Chan<sup>3</sup>, Celine K. Vuong<sup>4,5</sup>, Bethany Dubois<sup>2,6</sup>, Binsen Li<sup>2,3</sup>, Kevin A. Murray<sup>1</sup>, Michael R. Sawaya<sup>1</sup>, Juli Feigon<sup>3</sup>, Douglas L. Black<sup>4</sup>, David S. Eisenberg<sup>1\*</sup> and Lin Jiang<sup>1,2\*</sup>

**Inhibiting the interaction between amyloid- $\beta$  (A $\beta$ ) and a neuronal cell surface receptor, LirB2, has been suggested as a potential route for treating Alzheimer's disease. Supporting this approach, Alzheimer's-like symptoms are reduced in mouse models following genetic depletion of the LirB2 homologue. In its pathogenic, oligomeric state, A $\beta$  binds to LirB2, triggering a pathway to synaptic loss. Here we identify the LirB2 binding moieties of A $\beta$  (<sup>16</sup>KLVFFA<sup>21</sup>) and identify its binding site on LirB2 from a crystal structure of LirB2 immunoglobulin domains D1D2 complexed to small molecules that mimic phenylalanine residues. In this structure, we observed two pockets that can accommodate the phenylalanine side chains of KLVFFA. These pockets were confirmed to be <sup>16</sup>KLVFFA<sup>21</sup> binding sites by mutagenesis. Rosetta docking revealed a plausible geometry for the A $\beta$ -LirB2 complex and assisted with the structure-guided selection of small molecule inhibitors. These molecules inhibit A $\beta$ -LirB2 interactions in vitro and on the cell surface and reduce A $\beta$  cytotoxicity, which suggests these inhibitors are potential therapeutic leads against Alzheimer's disease.**

Aggregated amyloid- $\beta$  (A $\beta$ ) is found in large amounts in the autopsied brains of Alzheimer's disease (AD) patients, and it is widely considered a key factor in triggering neural degeneration in AD<sup>1,2</sup>. The long-standing amyloid cascade hypothesis has been challenged in recent years by the lack of correlation between A $\beta$  accumulation and cognitive impairment in elderly patients and the better correlation between histopathological changes of neurofibrillary tangles (aggregation of tau) and loss of cognition<sup>3-5</sup>. However, three major findings continue to support the hypothesis: A $\beta$  overproduction is found in nearly all familial forms of AD<sup>6,7</sup>, the oligomeric form of A $\beta$  is toxic to neurons<sup>8-10</sup>, and overexpression of A $\beta$  and APP (amyloid precursor protein) mutants in animal models leads to the development of AD-related phenotypes<sup>11,12</sup>. Recent AD-related studies continue to support the key role of A $\beta$ <sup>13,14</sup>.

Extensive work has focused on developing inhibitors of A $\beta$  toxicity as potential therapeutic drugs for AD. Most of these target A $\beta$  aggregation<sup>15-17</sup>, reduce the production of A $\beta$  through inhibition of  $\beta$ - or  $\gamma$ -secretase<sup>18-20</sup>, or reduce A $\beta$  levels through immunotherapy<sup>21,22</sup>. Recent studies suggest that one or more high-affinity protein receptors on the neuronal cell surface, such as cellular prion protein (PrP<sup>C23</sup>) and ephrin type B receptor 2 (EphB2<sup>24</sup>), are responsible for the recruitment of A $\beta$  oligomers and subsequent neurotoxicity<sup>25</sup>. These findings have sparked interest in illuminating the molecular mechanism of A $\beta$ -receptor recognition, with the hope that this information will lead to the development of new, effective AD therapeutics that inhibit the interaction of A $\beta$  with neuron cell receptors.

Among all these cell surface A $\beta$  receptors<sup>25</sup>, LirB2 is one of a few receptors that are reported to be promising therapeutic targets for

the treatment of AD, based on the observation that genetic depletion of the murine homologue, PirB (PirB<sup>-/-</sup>), rescues A $\beta$ -induced AD-related phenotypes in multiple model systems from cultured cortical neurons to transgenic mice, including recognition memory defects in APP/PS1 mice<sup>26</sup>. The two amino-terminal extracellular immunoglobulin domains (D1D2) of LirB2 and its murine homologue PirB selectively bind A $\beta$  oligomers with nanomolar affinity. LirB2 protein is detected in human brains of both AD patients and non-AD adults, with no significant difference in expression level, but its downstream signalling is altered in AD brains, implicating LirB2 in A $\beta$ -dependent synaptic loss<sup>26</sup>. Here, we identify the binding moieties of both A $\beta$  oligomers and LirB2 and present a model for their interaction. Based on the structural model, we designed A $\beta$ -LirB2 interaction inhibitors by computationally selecting molecules to compete with A $\beta$  for the LirB2 binding sites. The resulting compounds inhibited the interaction between oligomeric A $\beta$  and LirB2 with up to high nanomolar  $K_i$  and low micromolar half maximum inhibitory concentration (IC<sub>50</sub>) values. They also showed the ability to inhibit LirB2-induced A $\beta$ -cell contact, and therefore to inhibit A $\beta$  cytotoxicity.

## Results

**Mapping the core region of A $\beta$  binding to the LirB2 D1D2 domains.** A 200-residue recombinant LirB2 segment spanning the D1 and D2 domains (LirB2 D1D2) was used in our study, and oligomeric human A $\beta$ <sub>1-42</sub> (A $\beta$ 42) was prepared by incubating 10  $\mu$ M A $\beta$ 42 at 37 °C overnight (Supplementary Fig. 1). LirB2 D1D2 selectively binds oligomeric A $\beta$ 42 as previously reported<sup>26</sup> (Supplementary Fig. 2).

<sup>1</sup>Departments of Chemistry and Biochemistry and Biological Chemistry, UCLA-DOE Institute and Howard Hughes Medical Institute, UCLA, Los Angeles, CA, USA. <sup>2</sup>Department of Neurology, Molecular Biology Institute and Brain Research Institute, UCLA, Los Angeles, CA, USA. <sup>3</sup>Department of Chemistry and Biochemistry, UCLA, Los Angeles, CA, USA. <sup>4</sup>Department of Microbiology, Immunology and Molecular Genetics, David Geffen School of Medicine, UCLA, Los Angeles, CA, USA. <sup>5</sup>Present address: Systems Neurobiology Laboratory, The Salk Institute for Biological Studies, La Jolla, CA, USA.

<sup>6</sup>Present address: Division of Applied Mathematics, Brown University, Providence, RI, USA. \*e-mail: [david@mbi.ucla.edu](mailto:david@mbi.ucla.edu); [jianglin@ucla.edu](mailto:jianglin@ucla.edu)

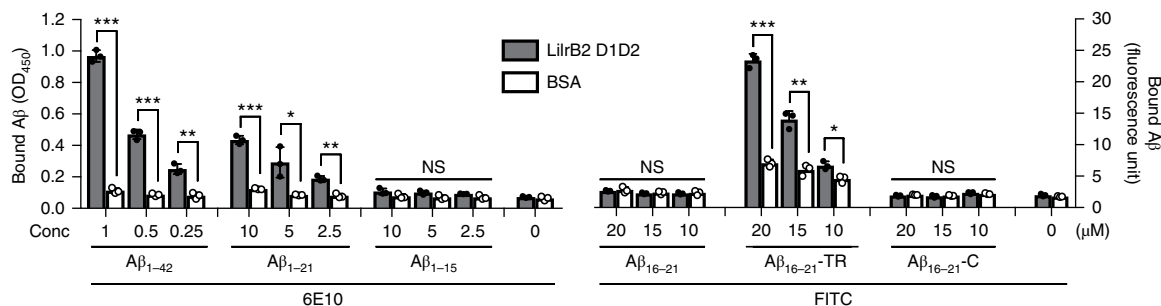


**Fig. 1 | The  $^{16}\text{KLVFFA}^{21}$  segment of A $\beta$  binds to LirB2 D1D2.** ELISA-based interaction assays of A $\beta$ 42 and its constituent segments. LirB2 D1D2 (grey bars) or bovine serum albumin as a negative control (BSA, white bars) was immobilized on ELISA plates, and incubated with A $\beta$  segments at the concentrations shown. The unbound segments were washed off and the amounts of bound A $\beta$  segments were measured by the A $\beta$ -specific antibody 6E10 and quantified by absorbance at 450 nm (left axis, optical density, OD<sub>450</sub>), or measured by the fluorescence signal of fluorescein (FITC) conjugated to the amino-termini of the segments and quantified by fluorescence units (right axis). Notice that for A $\beta$ <sub>1-42</sub>, A $\beta$ <sub>1-21</sub> and A $\beta$ <sub>16-21</sub>-TR, the amounts of A $\beta$  segments bound to LirB2 D1D2 were significantly higher than that to BSA, indicating interaction between these segments and LirB2 D1D2. The absence of KLVFFA from the weak binder A $\beta$ <sub>1-15</sub>, as well as its presence in the stronger binders A $\beta$ <sub>1-21</sub> and A $\beta$ <sub>16-21</sub>-TR (sequence KLVFFAPDGKLVFFA), indicate that  $^{16}\text{KLVFFA}^{21}$  is the key segment of A $\beta$  that binds to LirB2. Segment sequences are shown in Supplementary Table 1. Data are presented as means  $\pm$  s.d. ( $n=3$  independent experiments). Two-sided  $t$ -tests were performed and detailed statistical analyses are reported in Supplementary Table 4. \* $P < 0.05$ ; \*\* $P < 0.005$ ; \*\*\* $P < 0.0005$ ; NS, not significant; conc, concentration.

To map the binding core of A $\beta$ , we developed an enzyme-linked immunosorbent assay (ELISA)-based interaction assay that enables high-throughput detection of the A $\beta$ -LirB2 interaction. We immobilized LirB2 D1D2 on an ELISA plate and measured the amount of bound A $\beta$  segments by A $\beta$ -specific antibodies or the fluorescence signal of fluorescein conjugated to the segments. We found the LirB2 D1D2 domains bind to A $\beta$ 42 and its amino-terminal moiety A $\beta$ <sub>1-21</sub>, but not to A $\beta$ <sub>1-15</sub> (Fig. 1 and Supplementary Table 1). We also found that the LirB2 D1D2 domains bind to A $\beta$ <sub>15-35</sub> but not A $\beta$ <sub>22-42</sub> (Supplementary Fig. 2). These results indicate that the A $\beta$  segment  $^{16}\text{KLVFFA}^{21}$ , which is also widely considered to be a key element of A $\beta$  aggregation<sup>27,28</sup>, is the core region that binds to LirB2 D1D2.

We then tested the interaction of LirB2 D1D2 with  $^{16}\text{KLVFFA}^{21}$  derived peptides. We did not detect binding of LirB2 D1D2 to the peptide that contains a single copy of  $^{16}\text{KLVFFA}^{21}$  (A $\beta$ <sub>16-21</sub>, Fig. 1). However, our experiment showed it did bind to a tandem repeat (TR) design of  $^{16}\text{KLVFFA}^{21}$  (A $\beta$ <sub>16-21</sub>-TR, sequence KLVFFAPDGKLVFFA, Fig. 1, Supplementary Table 1). The binding we observed with the tandem repeats was not due to introduction of the Pro-Asp-Gly linker between the two  $^{16}\text{KLVFFA}^{21}$  copies, because the control peptide with a single copy of  $^{16}\text{KLVFFA}^{21}$  and the linker (A $\beta$ <sub>16-21</sub>-C, sequence KLVFFAPDG) did not bind to LirB2 D1D2 (Fig. 1). These results suggest that two copies of  $^{16}\text{KLVFFA}^{21}$  represent a minimal A $\beta$  oligomer and the core epitope for LirB2 binding. Moreover, the observation that the tandem repeat but not the single copy of  $^{16}\text{KLVFFA}^{21}$  binds to LirB2 suggests that LirB2 recognizes a particular conformation in addition to the primary amino acid sequence. We hypothesize that the antiparallel dimer of  $^{16}\text{KLVFFA}^{21}$ , rather than a single copy, readily assembles into a minimal oligomer, reasoning that the tandem linkage lowers the entropy barrier to oligomer formation (see Discussion).

#### Crystal structure of LirB2 D1D2 complexed with benzamidine.

We mixed LirB2 D1D2 with various A $\beta$  segments and screened for crystals, and we determined the crystal structure of LirB2 D1D2 mixed with A $\beta$ <sub>14-23</sub> at 2.1 Å resolution (Supplementary Table 2). In this structure, no density for the A $\beta$  segment was found, which is consistent with no detectable binding of  $^{16}\text{KLVFFA}^{21}$  monomer to LirB2 D1D2. Instead we found four benzamidine (Ben) molecules (Fig. 2a), which were used as an additive for crystal optimization. The presence and positions of the benzamidine molecules were determined by inspection of difference electron density maps ( $F_o - F_c$ , Supplementary Fig. 3) and the surrounding environment

(Fig. 2b,c). The chemical structure of benzamidine is similar to that of phenylalanine (Fig. 2a), so it mimics the binding of phenylalanine from the  $^{16}\text{KLVFFA}^{21}$  binding core of A $\beta$ . We chose the binding pockets of Ben 3 and 4 for further investigation because of the following observations. First, the binding pockets of Ben 3 and 4 are close to each other (separated by 7.5 Å) and are both located in the groove between the D1 and D2 domains (Fig. 2a). Given that at least two copies of  $^{16}\text{KLVFFA}^{21}$  are required to bind to LirB2 (Fig. 1) and each copy has two phenylalanines, it is likely that the binding sites for  $^{16}\text{KLVFFA}^{21}$  on LirB2 have two phenylalanine binding pockets close to each other. Second, most residues comprising the Ben 3 and 4 binding pockets are hydrophobic, with geometry suitable for binding bulky hydrophobic residues such as phenylalanine (Ile<sup>154</sup>, Tyr<sup>199</sup>, Pro<sup>204</sup>, Tyr<sup>205</sup> and Trp<sup>207</sup> for Ben 3 and Val<sup>38</sup>, Cys<sup>156</sup>, Pro<sup>164</sup>, Cys<sup>166</sup> and Trp<sup>207</sup> for Ben 4) (Fig. 2a-c). Hydrogen bonding (Ben 3 with Gly<sup>51</sup> and Asn<sup>168</sup>; Ben 4 with Asp<sup>36</sup>) and crystal lattice contacts (Ben 3 with Gly<sup>51</sup> and Ben 4 with Leu<sup>53</sup>) also stabilize benzamidine binding, but are minor contributors and appear unnecessary for binding phenylalanine. Third, Asp<sup>36</sup> and other negatively charged residues are located adjacent to the groove (Supplementary Fig. 3), close enough to neutralize the positive charge of Lys<sup>16</sup> of  $^{16}\text{KLVFFA}^{21}$  and further stabilize its binding. Fourth, by superimposing our complex on the ligand-free LirB2 D1D2 structure (PDB ID 2GW5<sup>29</sup>), we found that, on ligand binding, the binding groove widens due to movement of the  $\beta$ -strand of residues 165–168. In addition, the loop composed of residues 159–164, which is disordered and lacking electron density in the ligand-free structure, becomes ordered and forms a protective cap over the binding groove (Supplementary Fig. 3). These slight conformational changes make this groove a better binding site for both benzamidine and presumably the A $\beta$  binding core. On the basis of this structural analysis, we hypothesized that the binding pockets of Ben 3 and 4 on LirB2 are the binding sites for  $^{16}\text{KLVFFA}^{21}$  of A $\beta$ ; in the following we provide support for this hypothesis by mutagenesis and Rosetta docking.

#### Validation of the binding sites of LirB2 by mutagenesis and Rosetta docking.

We designed three LirB2 mutations to validate the putative binding sites for A $\beta$ . We first chose Asn<sup>168</sup> and Val<sup>38</sup>, whose side chains participate in the Ben 3 and 4 pockets, respectively (Fig. 2b,c). We mutated both to tryptophan to block these two pockets by creating steric hindrance with the ligands (Supplementary Fig. 3). We also designed the D36G mutation to target Asp<sup>36</sup>, which

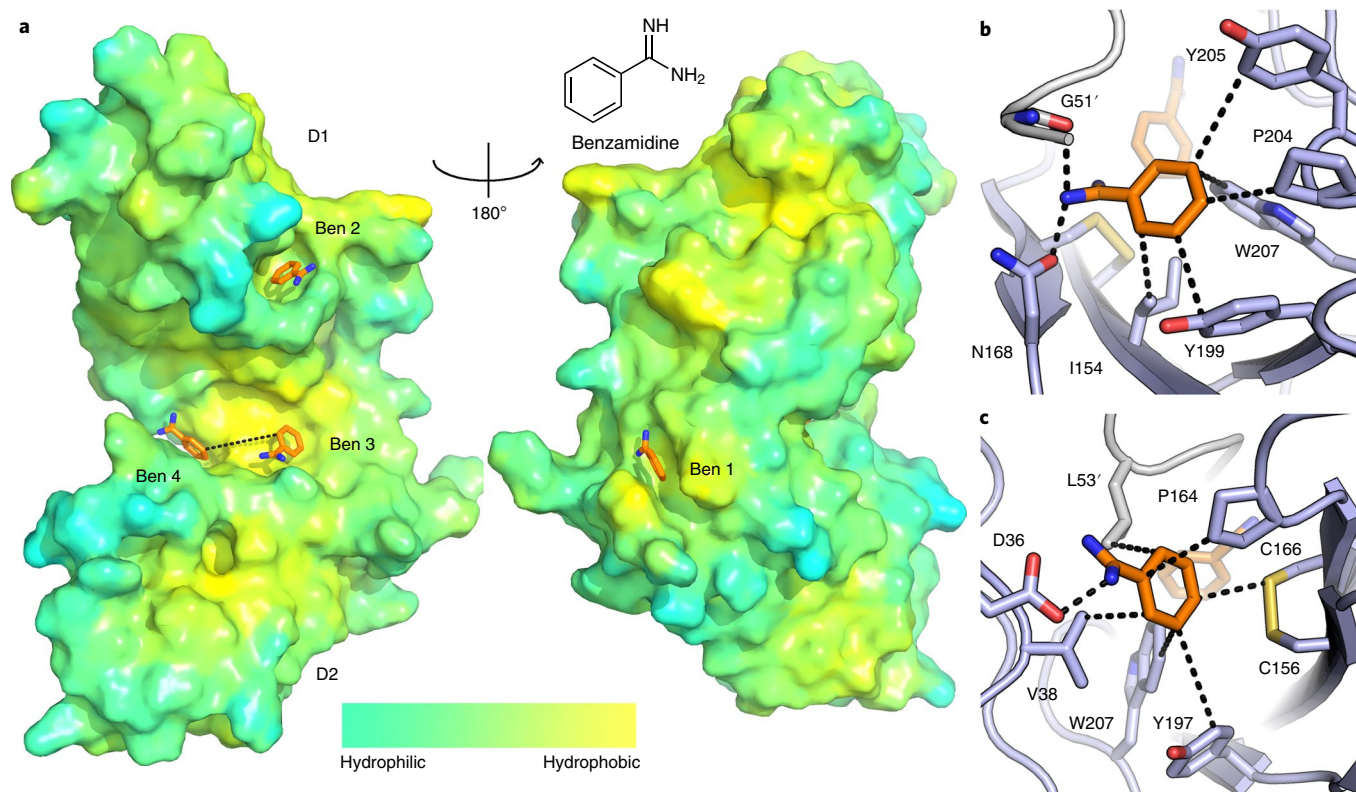


**Fig. 2 | Crystal structure of LiltrB2 D1D2 complexed with benzamidine.** **a**, Overview of the structure of LiltrB2 D1D2 (shown as a surface model, coloured by hydrophobicity) complexed with benzamidine (Ben 1 to 4, shown as sticks). The chemical structure of benzamidine is shown top right. The black dashed line between Ben 3 and Ben 4 represents 7.5 Å. Hydrophobicity ranges from  $-1.7$  (hydrophilic) to  $+3.7$  (hydrophobic). Notice that the binding pockets of Ben 3 and Ben 4 are located at the groove between LiltrB2 domains D1 and D2, and the groove has an extended hydrophobic surface. **b, c**, Detailed interaction of Ben 3 (**b**) and Ben 4 (**c**) with LiltrB2. LiltrB2 is shown as a cartoon and the side chains of the residues involved in benzamidine binding are shown as sticks. Black dashed lines represent distances between 2.4 Å and 4.8 Å.

putatively neutralizes the negative charge of Lys<sup>16</sup> of A $\beta$ . The three resulting mutant proteins, LiltrB2 D1D2 D36G, V38W and N168W, bound significantly lower amounts of full-length A $\beta$  as well as the <sup>16</sup>KLVFFA<sup>21</sup> tandem repeat (A $\beta$ <sub>16-21</sub>-TR) compared to wild type at the same loading concentration in ELISA-based interaction assays (Fig. 3a and Supplementary Fig. 4). Size exclusion chromatography shows that all three mutants elute at the same retention volume as wild type (Supplementary Fig. 4), and <sup>1</sup>H-<sup>15</sup>N-HSQC spectra show that these mutants have similar chemical shift patterns as wild type (Supplementary Fig. 4), which suggests that the diminished strength of these interactions is not due to changes in overall folding or the aggregation state of LiltrB2. These results indicate that blocking Ben 3 and 4 binding pockets by single mutations diminishes the binding of LiltrB2 for both full-length A $\beta$  and the <sup>16</sup>KLVFFA<sup>21</sup> tandem repeat. Therefore, these results support our hypothesis that Ben 3 and 4 binding pockets are the binding sites for <sup>16</sup>KLVFFA<sup>21</sup> in the tandem repeat and in full-length A $\beta$ .

To further validate the binding sites on LiltrB2 and to develop a model of A $\beta$ -LiltrB2 interaction, we applied Rosetta flexible peptide docking<sup>30</sup> to dock the <sup>16</sup>KLVFFA<sup>21</sup> segment to LiltrB2 D1D2. We used our crystal structure shown in Fig. 2 as a starting model for LiltrB2. An antiparallel  $\beta$ -sheet unit was taken from the crystal structure of the <sup>16</sup>KLVFFA<sup>21</sup> steric zipper (PDB ID 3OW9<sup>28</sup>) to represent a minimal  $\beta$ -sheet conformation of oligomeric A $\beta$ <sup>31</sup>, and the tandem repeat of A $\beta$ <sub>16-21</sub>-TR (see Discussion). During docking simulations, we confined KLVFFA to contact three key residues (Asp<sup>36</sup>, Val<sup>38</sup> and Asn<sup>168</sup>) that we identified as important for A $\beta$  binding in our mutagenesis experiments. To minimize the influence of the starting orientation of the peptide, we placed two strands of KLVFFA away

from the groove between the D1 and D2 domains (putative binding site) in a random orientation. Notably, we imposed no restraints to occupy the putative binding pockets identified in our crystal structure with benzamidine. For each starting conformation, 50,000 models were generated and the top 500 models with favourable Rosetta energies were further refined by energy optimization. After refinement, the five models ranked by Rosetta energies<sup>32</sup> and shape complementary<sup>33</sup> were selected for visual inspection. We found one model with two phenylalanine residues located within the binding pockets of Ben 3 and 4 (Fig. 3b-d). In this model, two independent KLVFFA molecules associated as an antiparallel  $\beta$ -sheet and docked in the groove between D1 and D2. Phe<sup>20</sup> and Phe<sup>19</sup> from separate molecules docked in the pockets of Ben 3 and 4, respectively. The root-mean-squared deviations of the aromatic rings between phenylalanine residues and benzamidine molecules are 2.3 Å. These docking results support our prediction of LiltrB2 binding sites and provide a putative model of A $\beta$ -LiltrB2 interaction. No other plausible A $\beta$  conformation was generated by our computational docking that fits two phenylalanines in these putative LiltrB2 binding sites.

**Structure-based design of A $\beta$ -LiltrB2 interaction inhibitors.** We designed A $\beta$ -LiltrB2 interaction inhibitors (ALIs) to occupy the binding sites on LiltrB2 and prevent A $\beta$  binding, as directed by our structural model of the A $\beta$ -LiltrB2 complex. Our approach, adapted from previous work<sup>34</sup>, combines knowledge of amyloid structures and computational screening to discover small molecules that interact with A $\beta$  fibrils and protect cells against their toxicity. We searched a compound library of  $\sim 32,000$  small molecules, including approved drugs, drugs in animal tests and clinical trials, and

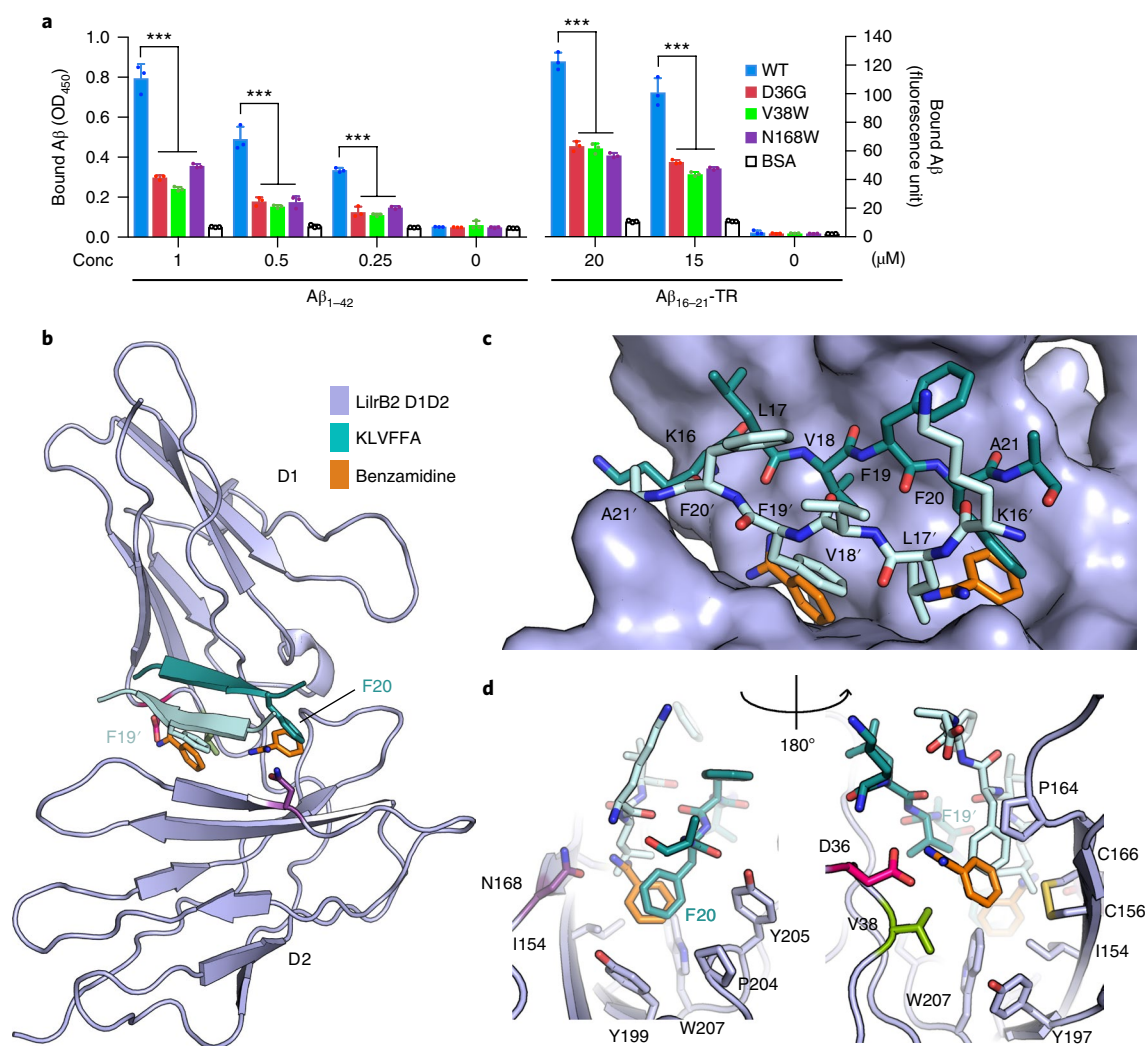


**Fig. 3 | Mutagenesis studies and Rosetta docking validate the A $\beta$  binding sites on LiltrB2.** **a**, ELISA-based interaction assays using wild-type LiltrB2 D1D2 (WT) or designed mutants. The same amount of LiltrB2 D1D2 WT (blue bars), D36G (red bars), V38W (green bars) and N168W (purple bars), as well as BSA (white bars), was immobilized on an ELISA plate (for loading control see Supplementary Fig. 4), and incubated with A $\beta$ <sub>1-42</sub> or A $\beta$ <sub>16-21</sub>-TR at concentrations indicated under each histogram. The amounts of bound A $\beta$ <sub>1-42</sub> were measured by antibody 6E10 and quantified by absorbance at 450 nm (OD<sub>450</sub>, left axis), and the amounts of bound A $\beta$ <sub>16-21</sub>-TR were measured by the fluorescence signal of fluorescein and quantified by fluorescence units (right axis). Data are presented as means  $\pm$  s.d. ( $n=3$  independent experiments,  $***P < 0.0005$ , ANOVA test); conc, concentration. For detailed statistical analysis see Supplementary Table 4. **b-d**, Model of two KLVFFA peptides binding to LiltrB2 D1D2 calculated by Rosetta docking. In this model, Phe<sup>20</sup> from one KLVFFA chain and Phe<sup>19</sup> from another chain bind to Ben 3 (**d**, left) and Ben 4 (**d**, right) pockets, respectively. Three residues tested in mutagenesis studies (Asp<sup>36</sup>, Val<sup>38</sup> and Asn<sup>168</sup>) were used as restraints in Rosetta docking. Residue colours correspond to the key in **a**.

natural products whose pharmacokinetic and/or toxicity profile is known (Supplementary Fig. 5 and Supplementary Methods). Small molecules that can potentially mimic the conformation of the aromatic rings of the ligand in our crystal structure were selected and docked to the binding pocket of LiltrB2. The compounds were then ranked by their predicted binding energy and the similarity between the docked model and the crystal structure. Finally, 12 top-ranking small molecules (ALI1–12) were chosen for experimental characterization based on their shape similarity, computational docking energy and potential to cross the blood–brain barrier (Supplementary Table 3).

We tested the inhibitory efficiency of all candidates by quantitative immunoprecipitation assays with LiltrB2 D1D2 and oligomeric A $\beta$ 42. At a molar ratio of 1:10:50 (LiltrB2:A $\beta$ :inhibitor), 9 of 12 candidates show inhibition of the A $\beta$ –LiltrB2 interaction with a lower A $\beta$  binding signal that was considered to be statistically significant compared to the controls with no inhibitor added (Fig. 4a). Six candidates

(ALI4, 5, 6, 7, 9 and 10) were selected for concentration-dependent studies, and all inhibited the A $\beta$ –LiltrB2 interaction in a dose-dependent manner (Fig. 4b and Supplementary Fig. 6). Their docking models, created by high-resolution Rosetta docking, were superimposed with benzamidine and are shown in Fig. 4c and Supplementary Fig. 6. Statistical analysis of the concentration-dependent studies shows that all six candidates have a high nanomolar to low micromolar  $K_i$  and low micromolar  $IC_{50}$  values (Fig. 4d). These results suggest that our structure-based design was successful in identifying small molecule inhibitors that block the A $\beta$ –LiltrB2 interaction in vitro.

**Tests of inhibitors by cell-based assays.** To test the inhibitors on cells, we transiently transfected HEK293T cells with full-length LiltrB2 with monomer red fluorescent protein (mRFP) conjugated at its carboxy terminus (LiltrB2–mRFP). We then tested the interaction of LiltrB2 with exogenously added oligomeric A $\beta$ 42 conjugated at its amino

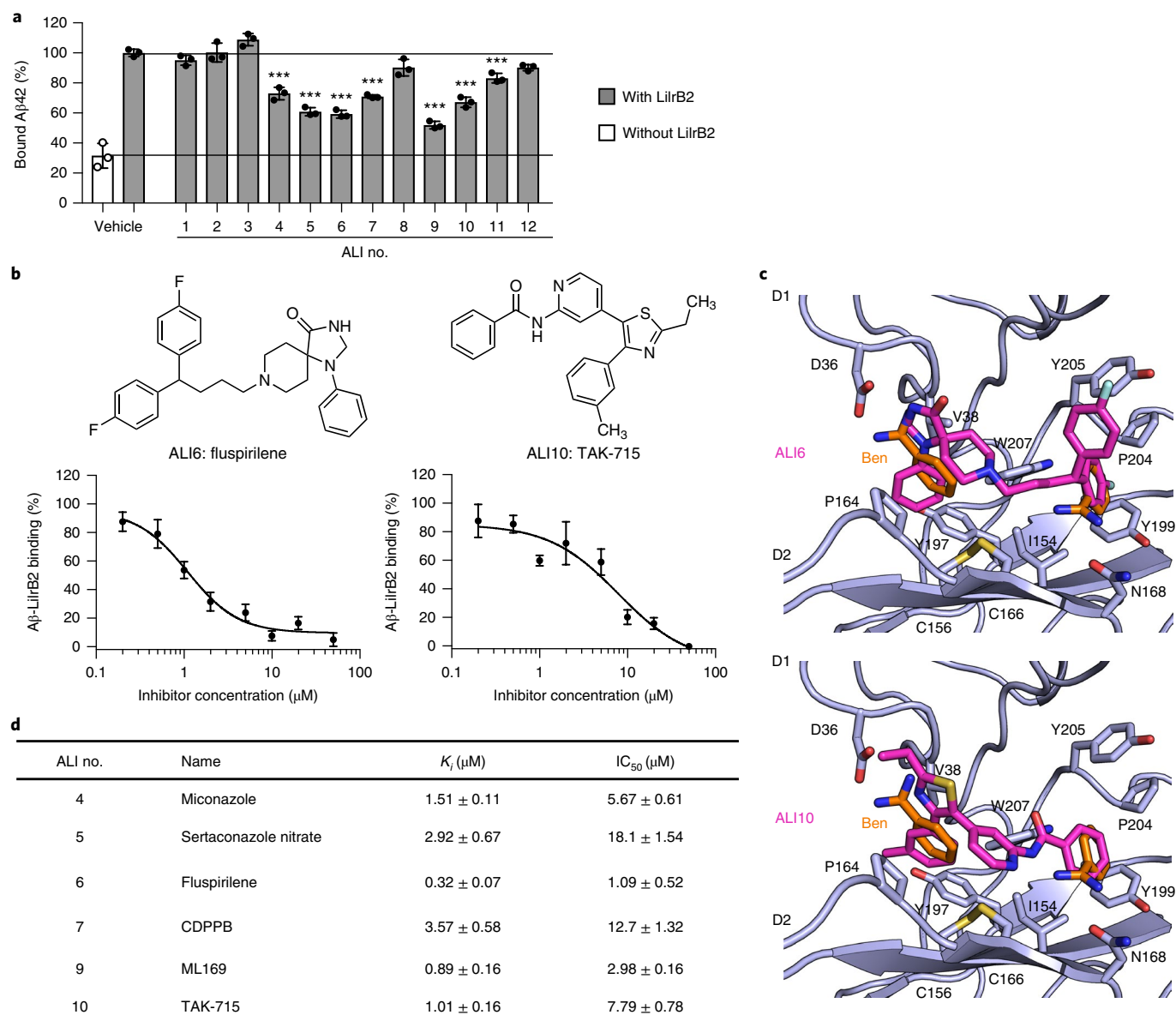


**Fig. 4 | Selected small molecules inhibit the A $\beta$ -LirB2 interaction in vitro.** **a**, Immunoprecipitation assays of A $\beta$ 42 with (black bars) or without (white bar) LirB2 D1D2. 1  $\mu\text{M}$  of A $\beta$ 42 and 100 nM of LirB2 D1D2 were mixed with 5  $\mu\text{M}$  of A $\beta$ -LirB2 inhibitors (ALI1-12) or equal amounts of DMSO (vehicle) and the amount of bound A $\beta$ 42 was quantified by ELISA. Data are presented as percentages relative to controls in which LirB2 and vehicle were added. Data are presented as means  $\pm$  s.d. ( $n=3$  independent experiments,  $***P < 0.0005$ , ANOVA test). For a detailed statistical analysis see Supplementary Table 4. **b**, Same immunoprecipitation assays using multiple concentrations of ALI6 (left) and ALI10 (right). ELISA absorbance values of samples without LirB2 were subtracted as background from those of samples with LirB2. Data are presented as percentages relative to the samples with LirB2 and vehicle. Percentage values of samples with inhibitors are plotted against concentration of inhibitors. The name and chemical structure of each inhibitor is shown at the top of each panel. **c**, Docking models of ALI6 (top) and ALI10 (bottom) binding to Ben 3 and 4 pockets. Residues involved in benzamidine binding are shown as stick models. **d**,  $K_i$  and  $\text{IC}_{50}$  values calculated from the data shown in **b** and Supplementary Fig. 6. In the immunoprecipitation assays in **b** and **d**, data are presented as mean  $\pm$  s.d.,  $n=3$  independent experiments.

terminus with fluorescein (FITC-A $\beta$ 42, Supplementary Fig. 7). HEK293T cells transfected with mRFP alone were used as negative control. After 3 h of incubation with FITC-A $\beta$ 42, we fixed and washed the cells, and found that cells transfected with mRFP bind only 13% of FITC-A $\beta$ 42 relative to cells transfected with LirB2-mRFP (Fig. 5a,b), consistent with previously reported results using HEK293 cells expressing LirB2 or PirB<sup>26</sup>. These results indicate that LirB2 induces A $\beta$ -cell interaction. When we added a 10  $\mu\text{M}$  concentration of our inhibitors to cells before adding FITC-A $\beta$ 42, we found the amount of bound A $\beta$ 42 was significantly reduced;

the lowest values were 27% (ALI10) and 29% (ALI6) relative to the controls in which no inhibitor was added (Fig. 5a,b). These results indicate that our selected small molecules inhibit the A $\beta$ -LirB2 interaction at the cellular level, and therefore inhibit LirB2-induced A $\beta$ -cell contact.

We selected candidate compound ALI6 to examine its effect on the cytotoxicity of A $\beta$ , because ALI6 exhibits the best score in the computational docking and the best inhibitory activity both in vitro and on cell levels. We transfected HEK293T cells with LirB2-mRFP and treated them with 500 nM oligomeric A $\beta$ 42 for

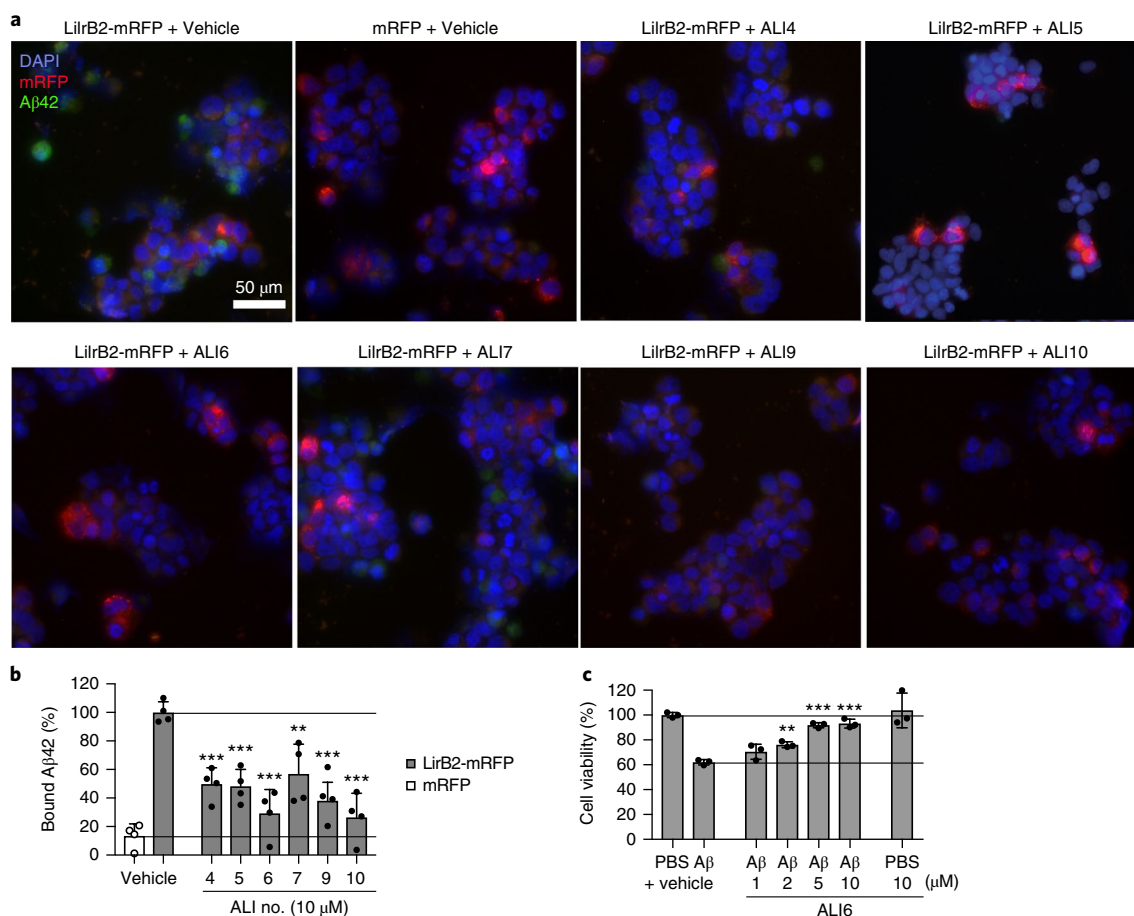


**Fig. 5 | Selected inhibitors block LirB2-induced cell attachment and inhibit toxicity of Aβ.** **a**, Fluorescent images of HEK293T cells transfected with LirB2-mRFP or mRFP (red), and treated with 500 nM fluorescein conjugated to Aβ42 (FITC-Aβ, green) and 10 μM selected Aβ-LirB2 inhibitors (or equal amounts of DMSO as vehicle control). DAPI, 4',6-diamidino-2-phenylindole. **b**, Quantification of the FITC-Aβ42 binding in **a**. Aβ42 binding was quantified as the integrated intensity of green fluorescence in each well, normalized to LirB2 expression level quantified as integrated intensity of red fluorescence in the same well (or normalized to cell confluency for cells transfected with mRFP), and then presented as a percentage relative to the controls, which are LirB2-mRFP transfected HEK293T cells treated with vehicle. Data are presented as means ± s.d. ( $n = 4$  independent experiments;  $**P < 0.005$ ,  $***P < 0.0005$ , ANOVA test). **c**, Cell viability (MTT) assays show that ALI6 reduces the toxicity of Aβ42. HEK293T cells transfected with LirB2-mRFP were treated with vehicle control or ALI6 at concentrations indicated under the histogram, and then 500 nM of oligomeric Aβ42 or PBS control was added. Cell viability is shown as a percentage relative to controls in which only PBS and vehicle are added. Data are presented as means ± s.d. ( $n = 3$  independent experiments;  $**P < 0.005$ ,  $***P < 0.0005$ , ANOVA test). For a detailed statistical analysis see Supplementary Table 4.

24 h. Cell viability (MTT) assays showed that 38% of cells were killed relative to controls in which the cells were incubated with PBS buffer solutions (Fig. 5c). Further cell viability assays established that ALI6 rescues the cells in a dose-dependent manner. When the cells were treated with ALI6 5 min before adding Aβ42, 1 μM ALI6 reduced the cell death to 30%, 2 μM ALI6 reduced the cell death to 24%, 5 μM ALI6 reduced the cell death to 8% and 10 μM ALI6 reduced the cell death to 7%. Moreover, 10 μM ALI6 in the absence of Aβ42 showed no effect on cell viability. These results suggest that ALI6 inhibits Aβ cytotoxicity.

**Validation of ALI6 with primary neurons.** Primary neuron models have been widely used to test Aβ cytotoxicity and the effect of Aβ inhibitors, and two known inhibitors of Aβ, curcumin<sup>35</sup> and (-)-epigallocatechin-3-gallate (EGCG)<sup>36</sup>, have been reported to rescue the neurotoxic effects of Aβ. We further validated the effect of ALI6 with mouse primary neurons. Cells from cortices dissected at embryonic day 15 were dispersed and cultured for 14 days in vitro (DIV14). Mouse cortical neurons have previously been shown to express PirB at DIV14<sup>37</sup>. Cells were then treated

with 500 nM FITC-Aβ42 to assess Aβ binding. We found that cells pretreated with 10 μM ALI6 bound  $39.0 \pm 20.5\%$  (mean ± s.d.) of FITC-Aβ42 compared to cells pretreated with the same amount of DMSO (Fig. 6a,b), indicating that ALI6 inhibits the binding of Aβ to neurons. The observation that ALI6 does not fully inhibit Aβ binding, even at a higher dose (50 μM ALI6 bound  $49.9 \pm 12.3\%$  FITC-Aβ42, Fig. 6b), indicates that there are Aβ receptors other than LirB2 on the neuronal cell surface, consistent with the observation of Aβ42 binding to neuron cells from PirB<sup>-/-</sup> mice at 50% the level of wild-type neurons<sup>26</sup>.

Although the binding of Aβ was not fully eliminated, we found that ALI6 is sufficient in inhibiting Aβ cytotoxicity in primary neurons, similar to curcumin<sup>35</sup> and EGCG<sup>36</sup>. Using terminal deoxynucleotidyl transferase-dUTP nick end labelling (TUNEL) assays to detect apoptotic DNA fragmentation, we found that  $50.1 \pm 4.3\%$  of the cells treated with Aβ42 and DMSO undergo cell death (Fig. 6c,d). When DMSO was substituted with same amount of ALI6 (5 μM), cell death dropped to  $16.5 \pm 8.9\%$ , equivalent to the vehicle control ( $11.9 \pm 11.4\%$ ) and ALI6 alone ( $11.0 \pm 11.6\%$ ). These results support the potential of ALI6 for rescuing Aβ-caused neuron damage.

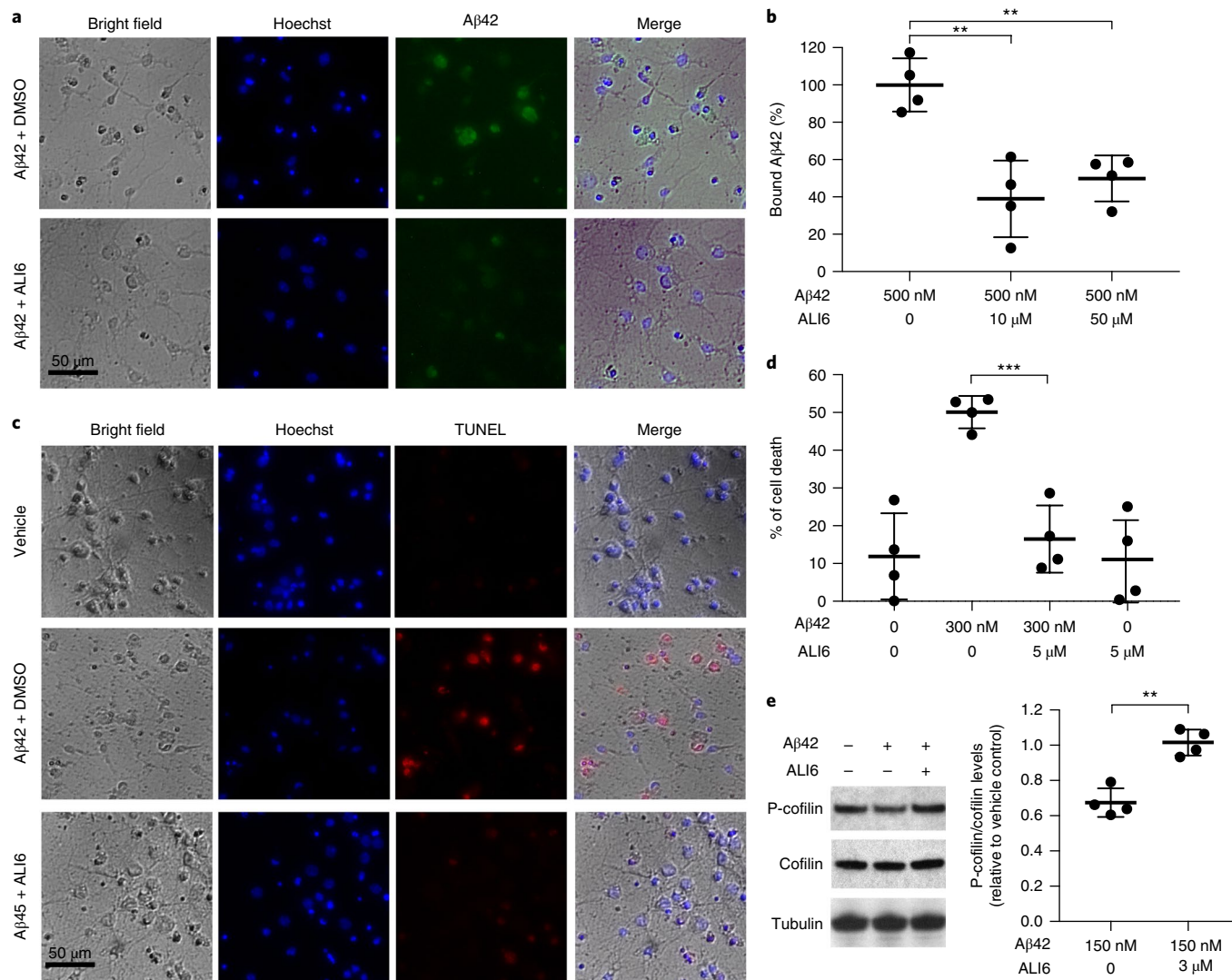


**Fig. 6 | Validation of ALI6 using primary neurons. a**, Bright-field and fluorescence images of primary neurons treated with 500 nM FITC-Aβ (green) and 10 μM ALI6 (or equal amounts of DMSO). **b**, Quantification of FITC-Aβ42 binding as in **a**. Aβ42 binding was quantified as the integrated intensity of green fluorescence in each well, normalized to cell confluency in the same well, and then presented as a percentage relative to cells treated with FITC-Aβ42 and DMSO (\*\**P* < 0.005, ANOVA test). **c**, Bright-field and fluorescence images of primary neuron cells treated with 300 nM Aβ42 and 5 μM ALI6 or equal amounts of DMSO, or treated with PBS and DMSO as vehicle control. Cell viability was measured by TUNEL assays, and dead cells are shown as red puncta. **d**, Quantification of TUNEL cell viability assays. Cell viability is shown as a percentage of cell death calculated as the number of red puncta divided by the number of blue puncta (Hoechst stain) (\*\*\**P* < 0.0005, two-sided *t*-test). **e**, Primary neuron cells were treated with 150 nM Aβ42 with 3 μM ALI6 or equal amounts of DMSO, and cofilin signalling levels were analysed by western blot (left). Anti-tubulin β-3 antibody detects neuronal tubulin and was used as a loading control. Quantification of cofilin phosphorylation (right) was calculated as the intensity of the phosphorylated cofilin band divided by the intensity of the cofilin band, and was normalized to cells treated with PBS and DMSO (vehicle control) (\*\**P* < 0.005, two-sided *t*-test). Data are presented as means ± s.d. (*n* = 4 independent experiments). For a detailed statistical analysis see Supplementary Table 4.

We further tested the effect of ALI6 on the downstream pathway of LiltrB2. A previous study proposed that Aβ–LiltrB2 interaction causes dephosphorylation of cofilin, an actin-depolymerizing factor, leading to eventual synapse loss<sup>26</sup>. Indeed, the same study showed the ratio of phosphorylated cofilin (p-cofilin) to total cofilin decreasing in primary neurons treated with Aβ. Here, we also found that on treatment with 150 nM Aβ42 for 1 h, the p-cofilin/cofilin level in primary neurons dropped to 67.5 ± 8.1% of the value seen in cells treated with vehicle alone (Fig. 6e). When pretreated with 3 μM ALI6, the p-cofilin/cofilin level was restored to 101.5 ± 7.4% relative to vehicle-treated cells. These results indicate ALI6 protects neurons from Aβ-induced changes in the cofilin signalling pathway, and further support the therapeutic potential of ALI6.

## Discussion

Our interaction assays confirm previous reports that LiltrB2 recognizes Aβ oligomers<sup>26</sup>, and suggest a molecular mechanism for the specificity of recognition. We first mapped the binding core to the segment <sup>16</sup>KLVFFA<sup>21</sup> of Aβ and tested two binding epitopes: a tandem repeat of <sup>16</sup>KLVFFA<sup>21</sup> (Aβ<sub>16–21</sub>-TR) designed to spontaneously self-assemble into an antiparallel β-sheet, and a single-copy peptide (Aβ<sub>16–21</sub>-C), which we presume remains single stranded in solution under the conditions tested due to an entropy barrier to oligomer formation. We found that LiltrB2 binds to the tandem repeat but not to the single strand (Fig. 1), suggesting that LiltrB2 recognizes an antiparallel β-sheet conformation specific to Aβ oligomers<sup>31</sup>.

Several lines of evidence support our hypothesis that Aβ<sub>16–21</sub>-TR is a better mimic of the full-length Aβ oligomer than is Aβ<sub>16–21</sub>-C.

$A\beta_{16-21}$ -TR has more  $\beta$ -strand content than  $A\beta_{16-21}$ -C, as indicated by a higher ellipticity (circular dichroism) value measured at 200 nm for the peptides linked to the 5x arginine tag (this tag was needed to achieve sufficient solubility) (Supplementary Fig. 2 and Supplementary Table 1). Analysis of the circular dichroism spectra also showed that the  $\beta$ -strand (antiparallel) content of  $A\beta_{16-21}$ -TR is higher (33%) than that of  $A\beta_{16-21}$ -C (28%). Moreover, when incubated at 37 °C at high concentration (2 mM),  $A\beta_{16-21}$ -TR formed fibrils but  $A\beta_{16-21}$ -C did not (Supplementary Fig. 2). Presuming that fibrillar and oligomeric species share common structural features, these results suggest that  $A\beta_{16-21}$ -TR better mimics the full-length  $A\beta$  oligomer, and explain our observation that it is a better epitope for LILRB2. Finally, the Rosetta docking experiments using as input the steric zipper structure of KLVFFA successfully generated a model that agrees with our LILRB2–benzamidine complex structure within the top 0.1% of Rosetta energy rankings. These results support our previous hypothesis that  $\beta$ -sheets are not only characteristic of amyloid fibres<sup>38</sup> but also of oligomers<sup>39,40</sup>.

The transient and heterogeneous nature of  $A\beta$  oligomers makes their structural elucidation extremely challenging. The observation that LILRB2 binds to  $A\beta$  oligomers with a wide range of sizes (Supplementary Fig. 2) also indicates the difficulty of characterizing the structure of an  $A\beta$  oligomer–LILRB2 complex. To gain insights into the structure of this complex, we first narrowed the binding core of  $A\beta$  to a six-residue segment (<sup>16</sup>KLVFFA<sup>21</sup>), and identified its binding site on LILRB2 through the structure of LILRB2 with a small molecule that mimics the phenylalanine side chains of the  $A\beta$  binding core. The binding sites were validated by mutagenesis and Rosetta docking, and then used for structure-based inhibitor design. Our results show that the LILRB2 D1D2–benzamidine complex structure we determined provides a platform sufficient for inhibitor development of the  $A\beta$ –LILRB2 interaction.

In addition to LILRB2, other putative  $A\beta$  receptors have been reported to bind  $A\beta$  oligomers and cause neuronal damage<sup>25</sup>. Our rationale for choosing LILRB2 as a target for inhibitor design is that an animal model shows that mice lacking PirB (the murine homologue of LILRB2) are immune to the damaging effects of  $A\beta$  in hippocampal long-term potentiation (LTP) and memory<sup>26</sup>. One reason to suppose that blocking only the LILRB2 receptor might be sufficient to inhibit  $A\beta$  toxicity is that blockade of one high-affinity  $A\beta$  receptor may sufficiently reduce the contact of  $A\beta$  with cells. This hypothesis is supported by the observation that  $A\beta_{42}$  oligomer binding to cultured cortical neurons from PirB<sup>-/-</sup> mice is diminished by about 50% relative to wild-type neurons<sup>26</sup>. In AD patients, this reduction may be sufficient to move the equilibrium from  $A\beta$ –cell contact to  $A\beta$  clearance<sup>41</sup>, thus inhibiting  $A\beta$ -triggered neuronal toxicity. Our cell viability assays on primary neurons support this hypothesis, which show ALI6 can almost completely block the effect of  $A\beta$  (Fig. 6d). Further study is required to identify the possibility that our inhibitor can also work on other  $A\beta$  receptors.

Compared to other AD drug development strategies that target  $A\beta$  aggregation<sup>15–17</sup> or bind monomeric  $A\beta$  with antibody<sup>42</sup>, targeting  $A\beta$  oligomer is advantageous because the inhibitor does not need to be added before  $A\beta$  aggregation. When testing the inhibition of  $A\beta$  cytotoxicity,  $A\beta$  monomer or aggregation targeting inhibitors need to be co-incubated with  $A\beta$  from the beginning of  $A\beta$  aggregation<sup>15</sup>, so presumably these inhibitors can only treat early-stage AD patients before massive  $A\beta$  aggregation forms. This may be part of the reason why solanezumab, an antibody targeting monomeric  $A\beta$ , failed in a recent clinical trial<sup>43</sup>. In comparison, all of our inhibition experiments were done by separately adding inhibitors and preformed  $A\beta$  oligomer, offering the possibility of treating patients that already have  $A\beta$  aggregation in their brains.

The structure-based approach has been shown to be a powerful tool for drug development<sup>5,44</sup>. In this study, we computationally

identified 12 candidate inhibitors by structure-guided selection. Nine out of 12 candidates show inhibition of the  $A\beta$ –LILRB2 interaction in vitro; six candidates were selected for further testing, and all of them exhibit low micromolar to high nanomolar  $K_i$  and  $IC_{50}$  values. These inhibitors eliminate the effects of  $A\beta$ –LILRB2 binding on the cell surface, and candidate ALI6 inhibits  $A\beta$  binding and cytotoxicity to primary neurons. Our results support the hypothesis that blocking this  $A\beta$ –receptor interaction is a potential way to inhibit  $A\beta$  toxicity and prevent neuron damage, and that LILRB2 is a promising therapeutic target. In addition, the compound library we used for computational inhibitor selection is composed of approved drugs, drugs in animal tests and clinical trials, and natural products whose pharmacokinetic and/or toxicity profile is known. During the inhibitor selection process, we also checked the potential of the selected compounds to cross the blood–brain barrier (Supplementary Table 3). This strategy ensures that our selected inhibitors, for example, ALI6, are safe for human use and are able to cross the blood–brain barrier. These properties make these inhibitors useful tools in further investigating the role of LILRB2 in the pathogenesis of AD, and qualifies them as promising candidates for expediting further AD drug development. We also note that the concentrations of inhibitors we used are high and might be difficult to achieve in vivo. Our proof-of-concept study provides several promising starting points for drug development, and further work is needed to improve the affinity of these inhibitors to increase their translational values.

## Methods

The methods and materials used in this study are available in the Supplementary Information.

**Reporting summary.** Further information on research design is available in the Nature Research Reporting Summary linked to this article.

## Data availability

The crystal structure reported here, LILRB2 D1D2 complexed with benzamidine, and the corresponding diffraction data have been deposited to the Protein Data Bank (PDB) with the accession code 6BCS. All other data are available upon reasonable request to the authors.

Received: 6 November 2017; Accepted: 28 August 2018;

Published online: 8 October 2018

## References

- Hardy, J. A. & Higgins, G. A. Alzheimer's disease: the amyloid cascade hypothesis. *Science* **256**, 184–185 (1992).
- Sheng, M., Sabatini, B. L. & Sudhof, T. C. Synapses and Alzheimer's disease. *Cold Spring Harb. Perspect. Biol.* **4**, a005777 (2012).
- Braak, H. & Braak, E. Alzheimer's disease: striatal amyloid deposits and neurofibrillary changes. *J. Neuropathol. Exp. Neurol.* **49**, 215–224 (1990).
- Nagy, Z. et al. Influence of the apolipoprotein E genotype on amyloid deposition and neurofibrillary tangle formation in Alzheimer's disease. *Neuroscience* **69**, 757–761 (1995).
- Seidler, P. M. et al. Structure-based inhibitors of tau aggregation. *Nat. Chem.* **10**, 170–176 (2018).
- Tanzi, R. E. & Bertram, L. Twenty years of the Alzheimer's disease amyloid hypothesis: a genetic perspective. *Cell* **120**, 545–555 (2005).
- Bettens, K., Sleegers, K. & Van Broeckhoven, C. Current status on Alzheimer disease molecular genetics: from past, to present, to future. *Hum. Mol. Genet.* **19**, R4–R11 (2010).
- Lambert, M. P. et al. Diffusible, nonfibrillar ligands derived from  $A\beta_{1-42}$  are potent central nervous system neurotoxins. *Proc. Natl Acad. Sci. USA* **95**, 6448–6453 (1998).
- Lesne, S. et al. A specific amyloid- $\beta$  protein assembly in the brain impairs memory. *Nature* **440**, 352–357 (2006).
- Li, S. et al. Soluble  $A\beta$  oligomers inhibit long-term potentiation through a mechanism involving excessive activation of extrasynaptic NR2B-containing NMDA receptors. *J. Neurosci.* **31**, 6627–6638 (2011).
- Hsiao, K. et al. Correlative memory deficits,  $A\beta$  elevation, and amyloid plaques in transgenic mice. *Science* **274**, 99–102 (1996).
- Ashe, K. H. & Zahs, K. R. Probing the biology of Alzheimer's disease in mice. *Neuron* **66**, 631–645 (2010).

13. Sorrentino, V. et al. Enhancing mitochondrial proteostasis reduces amyloid- $\beta$  proteotoxicity. *Nature* **552**, 187–193 (2017).
14. Zhu, B. et al. ER-associated degradation regulates Alzheimer's amyloid pathology and memory function by modulating  $\gamma$ -secretase activity. *Nat. Commun.* **8**, 1472 (2017).
15. Cheng, P. N., Liu, C., Zhao, M., Eisenberg, D. & Nowick, J. S. Amyloid  $\beta$ -sheet mimics that antagonize protein aggregation and reduce amyloid toxicity. *Nat. Chem.* **4**, 927–933 (2012).
16. Man, B. Y.-W. et al. Group 9 metal-based inhibitors of  $\beta$ -amyloid (1–40) fibrillation as potential therapeutic agents for Alzheimer's disease. *Chem. Sci.* **2**, 917 (2011).
17. Ehrnhoefer, D. E. et al. EGCG redirects amyloidogenic polypeptides into unstructured, off-pathway oligomers. *Nat. Struct. Mol. Biol.* **15**, 558–566 (2008).
18. Dovey, H. F. et al. Functional  $\gamma$ -secretase inhibitors reduce  $\beta$ -amyloid peptide levels in brain. *J. Neurochem.* **76**, 173–181 (2001).
19. Evin, G. Future therapeutics in Alzheimer's disease: development status of BACE inhibitors. *BioDrugs* **30**, 173–194 (2016).
20. Mitani, Y. et al. Differential effects between  $\gamma$ -secretase inhibitors and modulators on cognitive function in amyloid precursor protein-transgenic and nontransgenic mice. *J. Neurosci.* **32**, 2037–2050 (2012).
21. Castillo-Carranza, D. L., Guerrero-Munoz, M. J. & Kaye, R. Immunotherapy for the treatment of Alzheimer's disease: amyloid- $\beta$  or  $\tau$ , which is the right target? *Immunotargets Ther.* **3**, 19–28 (2014).
22. Sevigny, J. et al. The antibody aducanumab reduces A $\beta$  plaques in Alzheimer's disease. *Nature* **537**, 50–56 (2016).
23. Lauren, J., Gimbel, D. A., Nygaard, H. B., Gilbert, J. W. & Strittmatter, S. M. Cellular prion protein mediates impairment of synaptic plasticity by amyloid- $\beta$  oligomers. *Nature* **457**, 1128–1132 (2009).
24. Cisse, M. et al. Reversing EphB2 depletion rescues cognitive functions in Alzheimer model. *Nature* **469**, 47–52 (2011).
25. Jarosz-Griffiths, H. H., Noble, E., Rushworth, J. V. & Hooper, N. M. Amyloid- $\beta$  receptors: the good, the bad, and the prion protein. *J. Biol. Chem.* **291**, 3174–3183 (2016).
26. Kim, T. et al. Human LirB2 is a  $\beta$ -amyloid receptor and its murine homolog PirB regulates synaptic plasticity in an Alzheimer's model. *Science* **341**, 1399–1404 (2013).
27. Luhrs, T. et al. 3D structure of Alzheimer's amyloid- $\beta$ (1–42) fibrils. *Proc. Natl Acad. Sci. USA* **102**, 17342–17347 (2005).
28. Colletier, J. P. et al. Molecular basis for amyloid- $\beta$  polymorphism. *Proc. Natl Acad. Sci. USA* **108**, 16938–16943 (2011).
29. Willcox, B. E. et al. Crystal structure of LIR-2 (ILT4) at 1.8 Å: differences from LIR-1 (ILT2) in regions implicated in the binding of the human cytomegalovirus class I MHC homolog UL18. *BMC Struct. Biol.* **2**, 6 (2002).
30. Raveh, B., London, N., Zimmerman, L. & Schueler-Furman, O. Rosetta FlexPepDock ab-initio: simultaneous folding, docking and refinement of peptides onto their receptors. *PLoS ONE* **6**, e18934 (2011).
31. Stroud, J. C., Liu, C., Teng, P. K. & Eisenberg, D. Toxic fibrillar oligomers of amyloid- $\beta$  have cross- $\beta$  structure. *Proc. Natl Acad. Sci. USA* **109**, 7717–7722 (2012).
32. Kuhlman, B. & Baker, D. Native protein sequences are close to optimal for their structures. *Proc. Natl Acad. Sci. USA* **97**, 10383–10388 (2000).
33. Lawrence, M. C. & Colman, P. M. Shape complementarity at protein/protein interfaces. *J. Mol. Biol.* **234**, 946–950 (1993).
34. Jiang, L. et al. Structure-based discovery of fiber-binding compounds that reduce the cytotoxicity of amyloid  $\beta$ . *eLife* **2**, e00857 (2013).
35. Huang, H. C., Chang, P., Dai, X. L. & Jiang, Z. F. Protective effects of curcumin on amyloid- $\beta$ -induced neuronal oxidative damage. *Neurochem. Res.* **37**, 1584–1597 (2012).
36. He, Y. et al. Prolonged exposure of cortical neurons to oligomeric amyloid- $\beta$  impairs NMDA receptor function via NADPH oxidase-mediated ROS production: protective effect of green tea (–)-epigallocatechin-3-gallate. *ASN Neuro.* **3**, e00050 (2011).
37. Syken, J., Grandpre, T., Kanold, P. O. & Shatz, C. J. PirB restricts ocular-dominance plasticity in visual cortex. *Science* **313**, 1795–1800 (2006).
38. Gremer, L. et al. Fibril structure of amyloid- $\beta$ (1–42) by cryo-electron microscopy. *Science* **358**, 116–119 (2017).
39. Liu, C. et al. Out-of-register  $\beta$ -sheets suggest a pathway to toxic amyloid aggregates. *Proc. Natl Acad. Sci. USA* **109**, 20913–20918 (2012).
40. Laganowsky, A. et al. Atomic view of a toxic amyloid small oligomer. *Science* **335**, 1228–1231 (2012).
41. Nalivaeva, N. N., Belyaev, N. D., Kerridge, C. & Turner, A. J. Amyloid-clearing proteins and their epigenetic regulation as a therapeutic target in Alzheimer's disease. *Front. Aging Neurosci.* **6**, 235 (2014).
42. Crespi, G. A., Hermans, S. J., Parker, M. W. & Miles, L. A. Molecular basis for mid-region amyloid- $\beta$  capture by leading Alzheimer's disease immunotherapies. *Sci. Rep.* **5**, 9649 (2015).
43. Abbott, A. & Dolgin, E. Failed Alzheimer's trial does not kill leading theory of disease. *Nature* **540**, 15–16 (2016).
44. Wang, S. et al. D4 dopamine receptor high-resolution structures enable the discovery of selective agonists. *Science* **358**, 381–386 (2017).

### Acknowledgements

The authors thank C. Shatz for providing the LirB2 plasmid. This work is based on research conducted at the Northeastern Collaborative Access Team beamlines, which are funded by the National Institute of General Medical Sciences from the National Institutes of Health (P41 GM103403). The Pilatus 6M detector on the 24-ID-C beamline is funded by a NIH-ORIP HEI grant (S10 RR029205). This research used resources from the Advanced Photon Source, a US Department of Energy (DOE) Office of Science User Facility operated for the DOE Office of Science by Argonne National Laboratory under contract no. DE-AC02-06CH11357. L.J. is supported by UCLA departmental recruitment funds. The authors also acknowledge NIH AG 054022 and DOE DE-FC02-02ER63421 for support.

### Author contributions

Q.C., D.S.E. and L.J. conceived and designed the experiments. Q.C., W.S.S., H.C., C.K.V., B.D. and B.L. performed the experiments. W.S.S., B.D., K.A.M. and L.J. performed computational docking and structure-guided selection of small molecules. H.C. and J.F. performed and analysed NMR experiments. B.L. and L.J. performed and analysed circular dichroism experiments. C.K.V. and D.L.B. cultured primary neurons. Q.C. and M.R.S. solved the structure of the LirB2 and benzamidine complex. All authors discussed the results and commented on the manuscript. Q.C., D.S.E. and L.J. analysed the data and co-wrote the paper.

### Competing interests

D.S.E. is an advisor and equity shareholder in ADDRx.

### Additional information

**Supplementary information** is available for this paper at <https://doi.org/10.1038/s41557-018-0147-z>.

**Reprints and permissions information** is available at [www.nature.com/reprints](http://www.nature.com/reprints).

**Correspondence and requests for materials** should be addressed to D.S.E. or L.J.

**Publisher's note:** Springer Nature remains neutral with regard to jurisdictional claims in published maps and institutional affiliations.

© The Author(s), under exclusive licence to Springer Nature Limited 2018

## Life Sciences Reporting Summary

Nature Research wishes to improve the reproducibility of the work we publish. This form is published with all life science papers and is intended to promote consistency and transparency in reporting. All life sciences submissions use this form; while some list items might not apply to an individual manuscript, all fields must be completed for clarity.

For further information on the points included in this form, see [Reporting Life Sciences Research](#). For further information on Nature Research policies, including our [data availability policy](#), see [Authors & Referees](#) and the [Editorial Policy Checklist](#).

### ▶ Experimental design

#### 1. Sample size

Describe how sample size was determined.

Sample sizes were chosen to be 3 or 4 because they are generally considered as sufficient for 96-well plate based experiments, and generated acceptable P values in statistic analysis.

#### 2. Data exclusions

Describe any data exclusions.

No data were excluded from the analysis.

#### 3. Replication

Describe whether the experimental findings were reliably reproduced.

All attempts at replication were successful.

#### 4. Randomization

Describe how samples/organisms/participants were allocated into experimental groups.

Randomization is not relevant to our study. No research animals, human research participants or clinical studies are involved in our study. The samples we used are aqueous solutions. The allocations of each sample were extracted from a single falcon tube, eliminating differences in sample preparation.

#### 5. Blinding

Describe whether the investigators were blinded to group allocation during data collection and/or analysis.

Blinding was not relevant to our study, because all experiments were done on 96-well plates and quantified by plate reader. No subjective analysis were required.

Note: all studies involving animals and/or human research participants must disclose whether blinding and randomization were used.

#### 6. Statistical parameters

For all figures and tables that use statistical methods, confirm that the following items are present in relevant figure legends (or the Methods section if additional space is needed).

- | n/a                      | Confirmed                           |  |
|--------------------------|-------------------------------------|--|
| <input type="checkbox"/> | <input checked="" type="checkbox"/> | The <u>exact</u> sample size ( $n$ ) for each experimental group/condition, given as a discrete number and unit of measurement (animals, litters, cultures, etc.)                                    |
| <input type="checkbox"/> | <input checked="" type="checkbox"/> | A description of how samples were collected, noting whether measurements were taken from distinct samples or whether the same sample was measured repeatedly.  |
| <input type="checkbox"/> | <input checked="" type="checkbox"/> | A statement indicating how many times each experiment was replicated   |
| <input type="checkbox"/> | <input checked="" type="checkbox"/> | The statistical test(s) used and whether they are one- or two-sided (note: only common tests should be described solely by name; more complex techniques should be described in the Methods section) |
| <input type="checkbox"/> | <input checked="" type="checkbox"/> | A description of any assumptions or corrections, such as an adjustment for multiple comparisons  |
| <input type="checkbox"/> | <input checked="" type="checkbox"/> | The test results (e.g. $p$ values) given as exact values whenever possible and with confidence intervals noted   |
| <input type="checkbox"/> | <input checked="" type="checkbox"/> | A summary of the descriptive statistics, including central tendency (e.g. median, mean) and variation (e.g. standard deviation, interquartile range)   |
| <input type="checkbox"/> | <input checked="" type="checkbox"/> | Clearly defined error bars   |

See the web collection on [statistics for biologists](#) for further resources and guidance.

## ► Software

Policy information about [availability of computer code](#)

### 7. Software

Describe the software used to analyze the data in this study.

Graphs were plotted in Excel 2016 (version 15.29.1), KI and IC50 was calculated using GraphPad Prism (version 7.0c). Statistical significance was calculated by online t test calculator GraphPad QuickCalcs. Diffraction data was indexed, merged and scaled with XDS and XSCALE (version May 1, 2016). Molecular replacement was performed with Phaser (version 2.5.5), and refinements were performed using Phenix (version 1.12.2829) and Coot (version 0.8.9.1). NMR spectra were processed with TopSpin (version 3.5 pl 2) and analyzed with Sparky (version 3.114). Computational docking was performed by Rosetta software package (version 3.5) and high-throughput docking was performed by Glide Maestro (version 5.6) in Schrödinger suite package. The CD spectra were analyzed by the online software BeStSel. The intensity of cofilin bands were measured by ImageJ (version 1.51j8). The cell confluency, integrated intensity of green and red fluorescence in each well was calculated by Celigo (version 4.1.3.0).

For all studies, we encourage code deposition in a community repository (e.g. GitHub). Authors must make computer code available to editors and reviewers upon request. The *Nature Methods* [guidance for providing algorithms and software for publication](#) may be useful for any submission.

## ► Materials and reagents

Policy information about [availability of materials](#)

### 8. Materials availability

Indicate whether there are restrictions on availability of unique materials or if these materials are only available for distribution by a for-profit company.

No unique materials were used.

## 9. Antibodies

Describe the antibodies used and how they were validated for use in the system under study (i.e. assay and species).

i) clone name, 6E10; provide supplier name, BioLegend (previously Convence); catalog number, SIG-39320; host species, mouse; application, ELISA, WB, IHC, IP; dilution, 1:5000; application reference (selected), 1. Thakker DR, et al. Intracerebroventricular amyloid-beta antibodies reduce cerebral amyloid angiopathy and associated micro-hemorrhages in aged Tg2576 mice. *Proc Natl Acad Sci USA* Feb 25, 2009. 2. Klyubin I, et al. Amyloid beta protein immunotherapy neutralizes Abeta oligomers that disrupt synaptic plasticity in vivo. *Nat Med* 11(5):556-61, 2005.

ii) clone name, 4G8; provide supplier name, BioLegend (previously Convence); catalog number, SIG-39200; host species, mouse; application, ELISA, WB, IHC, IP; dilution, 1:1000; application reference (selected), 1. Thakker DR, et al. Intracerebroventricular amyloid-beta antibodies reduce cerebral amyloid angiopathy and associated micro-hemorrhages in aged Tg2576 mice. *Proc Natl Acad Sci USA* Feb 25, 2009. 2. Kimura N, et al. Age-related changes of intracellular Abeta in cynomolgus monkey brains. *Neuropath Appl Neurobiol* 31(2):170-80, 2005.

iii) clone name,  $\beta$  37-42; provide supplier name, Millipore Sigma; catalog number, AB5306; host species, rabbit; application, ELISA, IH(P); dilution, 1:500; application reference (selected), 1. Marksteiner, J; Humpel, C. Beta-amyloid expression, release and extracellular deposition in aged rat brain slices. *Molecular psychiatry* 13 939-52 2008. 2. Takashi Togo, Dennis W Dickson, Takashi Togo, Dennis W Dickson. Tau accumulation in astrocytes in progressive supranuclear palsy is a degenerative rather than a reactive process. *Acta neuropathologica* 104 398-402 2002

iv) name, Anti-Mouse IgG (whole molecule)-Peroxidase antibody; provide supplier name, Sigma-Aldrich; catalog number, A4416; dilution, 1:5000.

v) name, Anti-Rabbit IgG (whole molecule)-Peroxidase antibody; provide supplier name, Sigma-Aldrich; catalog number, A0545; dilution, 1:5000.

vi) name, Cofilin (D3F9) XP Rabbit mAb #5175; provide supplier name, Cell Signaling Technology; catalog number, 5175S; host species, rabbit; application, FC/FACS, ICC, IF, IHC, WB; dilution, 1:1000; application reference (selected), Megaw R. et al., Gelsolin dysfunction causes photoreceptor loss in induced pluripotent cell and animal retinitis pigmentosa models. *Nature Communications*, 2017.

vii) name, phospho-Cofilin (Ser3) (77G2) Rabbit mAb #3313; provide supplier name, Cell Signaling Technology; catalog number, 3313S; host species, rabbit; application, IF and WB; dilution, 1:500; application reference (selected), Megaw R. et al., Gelsolin dysfunction causes photoreceptor loss in induced pluripotent cell and animal retinitis pigmentosa models. *Nature Communications*, 2017.

viii) name, Anti-Tubulin  $\beta$ -3 (TUBB3) antibody; provide supplier name, BioLegend; catalog number, 802001; host species, rabbit; clone name, Poly18020; dilution, 1:5000; application reference (selected) Feuer R, et al. 2005. *J. Neurosci.* 25(9):2434-44. Mozzetti S, et al. 2005. *Clin. Cancer Res.* 11(1):298-305.

## 10. Eukaryotic cell lines

- State the source of each eukaryotic cell line used.
- Describe the method of cell line authentication used.
- Report whether the cell lines were tested for mycoplasma contamination.
- If any of the cell lines used in the paper are listed in the database of commonly misidentified cell lines maintained by [ICLAC](#), provide a scientific rationale for their use.

HEK293T cell line was from Prof. Samuel W. French's lab at UCLA

None of the cell lines used were authenticated by us

None of the cell lines used were tested for mycoplasma contamination by us

No commonly misidentified cell lines were used

## ► Animals and human research participants

---

Policy information about [studies involving animals](#); when reporting animal research, follow the [ARRIVE guidelines](#)

### 11. Description of research animals

Provide details on animals and/or animal-derived materials used in the study.

Male and female embryos (embryonic day 15) from pregnant CD-1 mouse dams.

Policy information about [studies involving human research participants](#)

### 12. Description of human research participants

Describe the covariate-relevant population characteristics of the human research participants.

The study did not involve human research participants